Macromolecules **2000,** *33,* 9407−9417

Perpendicular Deformation of a Near-Single-Crystal Triblock Copolymer with a Cylindrical Morphology. 2. TEM

Christian C. Honeker and Edwin L. Thomas*

Department of Materials Science & Engineering, Massachusetts Institute of Technology,
77 Massachusetts Avenue, Room 13-5094, Cambridge, Massachusetts 02139

Received April 3, 2000; Revised Manuscript Received September 25, 2000

ABSTRACT: A poly(styrene-*block*-isoprene-*block*-styrene) (SIS) triblock copolymer with a polystyrene (PS) cylinder morphology was globally oriented via roll-casting. Transmission electron microscopy (TEM) was used to assess the quality of orientation. The roll-casting process produces films with near-single-crystal-like orientation. Large strain deformation was applied perpendicular to the cylinder axis and retained by irradiating the sample with high energy electrons. TEM of sections viewed parallel and perpendicular to the cylinder axis provided real space information on the deformed morphology. For views parallel to the cylinder axis, the initial hexagonal packing of the cylinders distorts into a faulted twinlike texture in which layers of cylinders are oriented at fixed angles with respect to the stretching direction (SD). These fault boundaries are separated by an average distance of about 0.1 μm at 180% deformation. Direct evidence for a chevron texture in which the cylinders kink and turn into the SD was observed at perpendicular incidence. Kink boundaries are separated by an average distance of about 5 μm at a strain of 180%. Optical transforms (OTs) of the TEM images as well as SAXS on deformed irradiated samples are used to directly connect the results to the dynamic SAXS described in a complementary paper.[1] A 3-D model of the deformed morphology summarizes the real space data self-consistently and provides the basis for an interpretation of the dynamic SAXS data.

1. Introduction

Strength in combination with high extensibility have long been properties associated with cross-linked (filled) rubbers. Processing of these materials is, however, energy intensive and irreversible. Thermoplastic elastomers (TPEs) embody these mechanical attributes with the ability to be processed as traditional thermoplastics. It is the nature of the reinforcing component which distinguishes TPEs from conventional filled and cross-linked rubbers. The rigid domain remains in intimate contact with the soft domain, but can be dissolved with the application of heat and/or solvent. This feature permits scrap material to be recycled; an additional advantage over cross-linked rubbers. Thus, TPEs are increasingly used to replace conventional vulcanates wherever large deformations are encountered and the demands of high temperature performance and/or solvent resistance are not too stringent.[2]

Although it has long been known[3] that the “hard” domains act in a way similar to reinforcing filler, the impact of hard domain morphology (including structural anisotropy) on mechanical properties particularly at large deformations is not so well understood.[4] Styrene/diene thermoplastic elastomers with a linear ABA glass/rubber/glass molecular architecture serve as model materials due to their well-characterized molecular and morphological structure.[5] A typical TPE at low styrene (30%) content with a cylinder morphology can be processed to give global orientation.[4] Such macroscopically oriented samples have led to the determination of the anisotropic compliance tensor at low strains for the cylinder morphology.[6] A relatively new processing technique, “roll-casting”, is used here to prepare films with long-range orientation.[7,8] This well-defined initial morphology provides a unique starting point from which the expected mechanically anisotropic behavior can be probed.

We provide direct microscopic information on the evolution of the microdomain morphology on a sample which is deformed normal to the cylinder axis to large strains. This information validates the SAXS-based interpretation presented in previous studies[1,9,10] as well as serves as the basis for construction of a 3-D model of the deformed morphology.[1] This real space model is then used to provide further insight into the mechanism of deformation perpendicular to the cylinder axis in this unique anisotropic nanocomposite. Understanding of the deformation process of a single grain is a necessary step in the elucidation of the deformation behavior of polygranular samples.

2. TEM Studies on Deformed Triblock Copolymer Morphologies

Attempts have been made to directly image the deformed morphology of thermoplastic elastomers via TEM, but no studies have been carried out on oriented cylinders deformed perpendicular to the cylinder axis to large deformations. A variety of sample preparation techniques have been used with varying degrees of success, but few have combined a well-characterized system consisting of a monodisperse block copolymer and a highly oriented initial morphology with a method to fix the deformed morphology before TEM section preparation. Here, we briefly review TEM investigations on the deformation of unoriented morphologies and then consider those on oriented systems.

2.1. TEM of Unoriented Polygranular Cylinders and Lamellae. Hendus et al.[11] in 1967 quiescently cast poly(styrene−butadiene−styrene) SBS (with 38% PS) from toluene. TEM and SAXS were performed on samples stretched to approximately 100%. Though the undeformed sample showed a chaotic, poorly ordered microdomain morphology, it was observed that the PS as well as the PB “bands” oriented themselves along the

10.1021/ma000594q CCC: $19.00

stretching direction. The spacings perpendicular and parallel to the stretching direction (SD) between the short PS domains decreased and increased, respectively. No special technique to fix the deformation in the sample before TEM preparation was mentioned, but the sample necked and retained some permanent deformation upon unloading.

A more systematic TEM investigation of the deformation process of KRATON 101 (a commercial SIS with 28 wt % PS) was carried out by Beecher et al.[12] Samples were prepared by casting from a variety of solvent systems as well as via compression molding. In hindsight, it is apparent that the solvent-induced morphology was poorly defined, but it was found that strings of PS spheres oriented themselves in the stretching direction and subsequently formed “V-shaped” patterns. It was also noted that the connected spheres separated into individual particles and that these distorted into ellipsoidal domains at higher deformations. Grains were observed in various states of deformation, suggesting an inhomogeneous deformation which would be expected from a sample undergoing necking with the consequent nonuniformity in strain distribution along the gage length. Nevertheless, the study was the first to attempt to describe the deformation process using a series of TEM micrographs at different amounts of stretch. As with many other studies,[13,14] this one suffered from the poor quality of starting materials (a commercial product with inevitable diblock and homopolymer impurities) as well as an ill-defined initial morphological state.

A closer connection between structure (sample morphology) and property (stress−strain curve) was provided by Fujimura et al.[15,16] in a SAXS and TEM study of unoriented SBS lamellae. The deformation process was assessed by 2-D SAXS patterns taken at various points along the stress−strain curve during a loading/unloading cycle. TEM images of permanently deformed specimens were used as snapshots, providing further support for the SAXS interpretation. At 85% permanent deformation, chevrons aligned with the SD were observed, whereas at 500% deformation, the PS domains had become highly fragmented. Although the study mentions the yielding and necking of the sample, again, no account is made of the impact on the SAXS data due to the consequent localization of the deformation. Thus, the morphological data cannot directly be mapped to a particular strain on the stress−strain diagram as the strain in the probed region is no longer directly determined by the macroscopic strain.

2.2. TEM of Oriented Systems. Keller and coworkers directly imaged oriented cylinders after deformation parallel to the cylinders axis using TEM.[17] Special care was taken in sample preparation. The oriented material was stored in the strained condition until the stress relaxed to zero. The permanently deformed sample was then OsO_4 stained and cryomicrotomed to yield sections of 500 Å or less in thickness. Convincing evidence that the cylinders not only remained aligned in the stretching direction but also broke up into short rodlets of 700−1100 Å length was obtained.

A recent TEM study on a commercial styrene−butadiene star-shaped block copolymer with a lamellar structure was conducted as a function of sample processing.[18] A molecular weight polydispersity of 2.7 and an (unknown) average arm-number polydispersity possibly accounted for the unusual observation of lamellae at only 25 wt % PS. Samples were injection- as well as compression-molded before tensile, fracture, and flexural experiments were carried out. TEM sections were taken near the fracture surface after specimen failure. A rapidly cooled compression-molded sample stretched normal the lamellae showed clear evidence of a zigzag (chevron) morphology just below the fracture surface. More recently, similar investigations on SBS/poly(methyl methacrylate-*block*-styrene) blends have been carried out.[19,20]

Common among many previous TEM investigations of deformed triblock copolymers is either the lack of a well-defined initial starting morphology or lack of a complementary technique with which local information gained via TEM can be extrapolated to the entire sample. Effectively fixing the deformed morphology has been a challenge. These shortcomings are addressed in a closely related investigation[21] of the response of a *globally* oriented lamellar system to deformation along three morphological directions: parallel with, perpendicular to, and at 45° to the lamellar normal. Synchrotron−SAXS and TEM, on samples fixed via electron irradiation, provided the experimental basis for a detailed account of the deformation mechanisms. Deformation parallel to the lamellae results in yielding and necking in which fragmented PS domains are drawn into the necked region, which subsequently behaves in a manner similar to a reinforced rubber. Perpendicular deformation causes the lamellae to undulate or kink into a symmetric chevron pattern. The rotation of the lamellae is shown to proceed affinely at a constant lamellar spacing. Deformation at 45° to the lamellar normal, on the other hand, gives rise to asymmetric kink boundaries. At the highest strains the PS domains rotate toward the stretching direction, a response anticipated for polygranular lamellar systems.

2.3. Organization of the Paper. This TEM investigation together with the SAXS investigation[1] provides local real space and global reciprocal space information on the deformed morphology from which a 3-D real space model is constructed. The quality of the initial undeformed morphology is assessed and examples of the types of defects that give rise to the arcing of the SAXS patterns of the initial undeformed structure are provided. TEM micrographs viewed in the perpendicular and parallel directions to the cylindrical axis of samples with 120% and 180% permanent deformation are presented and discussed. The morphology was captured by irradiating stretched samples via high energy electrons in order to induce the rubber phase to cross-link and stiffen. A discussion of the 3-D model of the highly deformed structure concludes the paper.

3. Experimental Section

3.1. Materials and Preparation. The material examined was a SIS triblock copolymer with block molecular weights of 15−72−15 kg/mol and a PS content of 29 wt %. Samples were oriented using the roll-casting technique.[8] Further details of molecular characterization and sample orientation are available[22] while the SAXS investigation corresponding to the present TEM study can be found in ref 1.

3.2. Sample Fixation. To fix the morphology in a particular deformation state for observation in the TEM, stretched samples were heavily cross-linked by irradiation with high energy electrons. Samples were held in a deformation stage under a high energy electron beam for a certain period and then unloaded. The final, permanent deformation was then

Table 1. Approximate Cross-Link and Scission Yields for Irradiated Polymers[a,b]

polymer	*G*(X)	*G*(S)	*G*(X)/*G*(S)
polystyrene	0.045	<0.018	2.5
natural rubber	1.1	0.22	6.25

[a] From ref 30. [b] Irradiation at room temperature under vacuum or inert atmosphere (nitrogen).

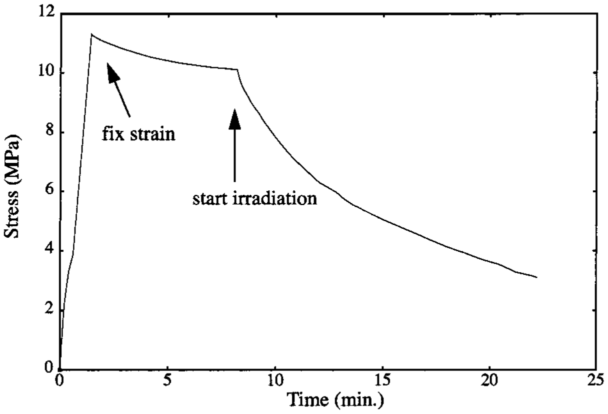

Figure 1. Stress−time history for a perpendicular stretch and irradiation experiment performed at Raychem (now Tyco Electronics). The sample was stretched to 620% strain, and after approximately 6 min of stress relaxation, an 0.8 MeV electron beam at a current of 1.2 mA was applied. Irradiation continued until break for a total dose of 410 kGy. The residual strain was measured to be approximately 120%.

recorded. This technique, though capable of "freezing-in" a significant amount of deformation, cannot prevent some relaxation.

The precondition for network formation under high energy irradiation is a higher coefficient for cross-linking (*G*(X)) than for chain scission (*G*(S)). For styrene−diene block copolymers, this condition is fulfilled (see Table 1).[23]

Two sets of experiments were carried out at two different electron beam facilities, Raychem (now Tyco Electronics) in Menlo Park, CA, and at MIT's High Voltage Lab (HVL). Samples with 120% and 180% permanent deformation were prepared at Raychem and at MIT HVL, respectively.

The Raychem experiments were carried out under more controlled conditions. Measurements of load history and dosage were made on samples stretched to various deformations. Beam currents of 1.2 and 5.0 mA at an accelerating voltage of 0.8 MeV were used. The electron flux had a Gaussian distribution but was relatively uniform over the sample footprint. Dosage was determined using low-density polyethylene (LDPE) films (approximately 0.5 mm thick) placed next to the sample during each run. The *trans*-vinylene unsaturation concentration was subsequently measured via FT-IR.[24,25] Liquid crystal temperature strips ($T_{\mathrm{range}} = 100-250$ °F in increments of 5 °F) were taped on the stretching frame to determine the maximum temperature reached during the irradiation experiment. Because of an air blower located on the scan horn, the frame never reached 100 °F (37.8 °C).

For the data presented in sections Section 5.1 and section 5.3, a sample was stretched to 620% strain and irradiated with 0.8 MeV electrons for approximately 15 min before the sample broke (Figure 1). The residual deformation was measured to be approximately 120%, while the total dose was approximately 410 kGy. Note that the residual strain immediately after unloading of a sample stretched to similar deformations and unloaded (Figure 9 in ref 1) is less than 40%. Thus, irradiation serves to capture about 20% of the total deformation as compared to 6% without.

Experiments conducted at Raychem provide stress-time histories during the course of the irradiation. Figure 1 demonstrates that there is an immediate and significant increase in the stress relaxation rate upon irradiation. The sample immediately turns white and fluoresces during irradiation. The radiation-induced chemical processes in these samples are thought to be quite complex and are beyond the objective of this study. The main molecular changes are, however, chain scission and cross-linking.

The MIT High Voltage Lab (HVL) irradiation experiments used a Van de Graaf generator at an energy of 2.6 MeV. Samples were held in a stretching jig at certain deformation and passed underneath the scan horn of the electron beam by a conveyer belt. Each pass delivered approximately 25 kGy (2.5 Mrad) dose to the sample. Dosages of up to 800 kGy (80 Mrad) were delivered in this way. The MIT HVL experiments captured larger amounts of deformation than those conducted at Raychem. However, the stress−time history for these samples could not be recorded. The data presented in sections 5.2 and 5.4 is from a sample stretched in the perpendicular direction to 410% strain and irradiated with 80 MRad. It was unloaded and found to retain 180% strain.

Large amounts of deformation in styrene−diene TPEs can be fixed via the high energy electron irradiation technique used here or by treatment with OsO_4 vapors.[15,16] Both methods cross-link the sample, though the physical processes involved are very different. The success of the method can be measured by the amount of strain retained upon unloading compared to the stretched state. Holding samples of SBS lamellae at deformations of 85% and 500% in OsO_4 vapors for 48 h resulted in permanent deformations of 64% and 200%,[15,16] respectively. In this study samples held at 600% and 400% retained 180% and 120% deformation, respectively. Considering the higher rubber content of the PS cylinder morphology, the high energy electron irradiation technique compares favorably with the OsO_4 staining technique.

3.3. TEM. Sections of the deformed and irradiated samples were microtomed using a Reichert-Jung Ultracut FC 4E at temperatures of −90 (knife) and −110 °C (sample) with a nominal section thickness of 70 nm. The sections were subsequently stained with OsO_4 vapors for 1−2 h and carbon coated.

TEM was carried out on a JEOL 200 CX using a tungsten filament. Standard conditions were: 200 keV accelerating voltage, 300 μm condenser aperture, 40 μm objective aperture, and a magnification between 7 and 37 k×. A rotate/tilt holder was used to vary the section normal with respect to the incident beam direction. The tilt axis was determined by depositing PS latex spheres on the section. By following the motion of the spheres as a function of tilt, the tilt axis at a particular magnification can be determined quite accurately.

Optical transforms (OTs) of the TEM negatives were performed using an optical diffractometer equipped with a HeNe laser with $\lambda = 633$ nm. Patterns were recorded on Polaroid 55 film. As a local technique, however, TEM is not suited to provide information about the *global* degree of order in the sample.

4. Initial Orientation

4.1. Perpendicular View. A TEM micrograph with the incident beam normal to the cylinder axis is shown in Figure 2. Although the average cylinder trajectory across the image is continuous, numerous defects which cause localized waviness to the cylinders are observed (an example is circled). These defects correspond to terminated cylinders and give rise to transverse edge dislocations. Some terminations may also be due to the clipping of certain cylinders which are nonplanar with the microtome section. The narrow dark bands normal to the cylinder axes (arrows in Figure 2) occur due to the displacement fields of pairs of oppositely-signed edge dislocations (pairs of dislocation dipoles). These defects manifest themselves in the SAXS data which show a 15° fwhm azimuthal misorientation about the *y* direction.[1]

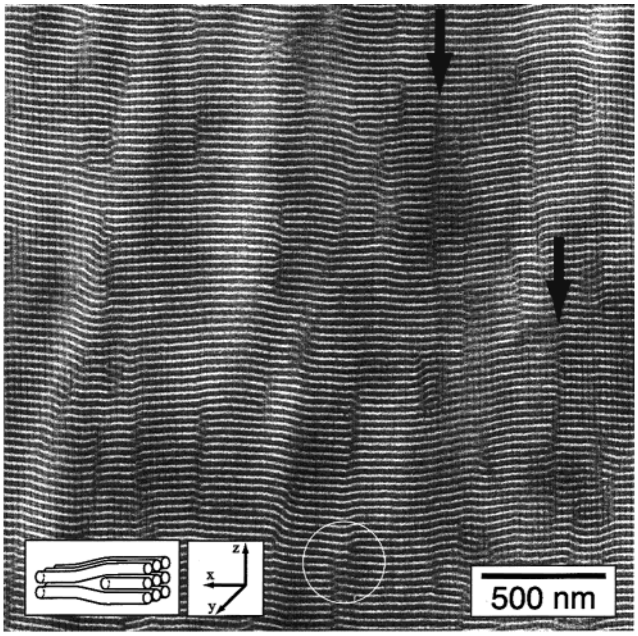

Figure 2. TEM of roll-cast SIS 15K−72K−15K at normal incidence. The rubber is stained dark with OsO$_4$. The PS cylinders are oriented along the flow field (horizontal), but contain groups of vertically aligned transverse edge dislocations (one representative circled) found in several dark bands (arrowed). These defects give rise to a slight waviness of the PS cylinders.

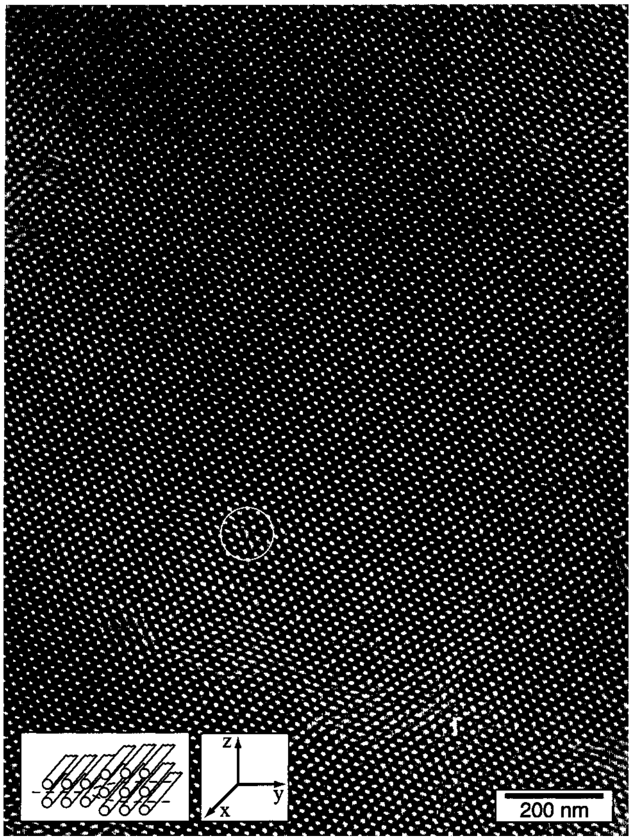

Figure 3. TEM micrograph of the undeformed SIS sample with the electron beam incident parallel to the cylinder axis. The field of view is part of a far larger grain showing a high degree of lateral registry. Viewing the figure at low angles along directions of cylinder close packing reveals axial edge dislocation defects (one representative circled).

4.2 Parallel View. TEM micrographs taken with the incident beam down the cylinder axis give direct information about the lateral degree of order in the hexagonal lattice (Figure 3). Axial tilt grain boundaries are the most common type of defect which can be found in roll-cast films of the cylinder morphology. An example of the rotational misalignment of grains of cylinders about their axes is shown in Figure 4. The center grain (β) is misoriented with respect to grain (α) by an angle of approximately 25°. The OTs confirm that grain (α) has the same relative orientation on either side of (β). OTs taken at the (α/β) and (β/α) interfaces show how a combination of misoriented grains can spread the intensity of a highly ordered hexagonal diffraction pattern into that observed experimentally (compare the OTs of Figure 4 with the SAXS pattern at 0% strain in Figure 8a of ref 1). SAXS yields a 10−13° fwhm axial misorientation about the *x* direction. Taken together, TEM views reveal an extremely well-ordered initial morphology with a high degree of both azimuthal and axial orientation.

5. Deformed Sample Morphology

The deformed SIS morphology was captured at strains of 120% and 180% under two different irradiation conditions. TEM was performed on sections cut so that the incident beam (viewing direction) was oriented both perpendicular and parallel to the original cylinder axis. We begin with the perpendicular view.

5.1. 120% Strain—Perpendicular View. TEM images of a sample with 120% permanent deformation viewed transverse to the cylinder axis are shown in Figure 5. The low magnification image shows that the PS cylinders have been bent into a chevron-like texture similar to kink bands with boundaries parallel to the deformation direction. Careful inspection of the boundaries (see Figure 6, parts a and d) shows that the PS cylinders are continuous across the boundary (coherent tilt boundary). On either side of the boundary, the PS cylinders remain parallel and at a fixed angle with respect to the deformation direction. The angle between the normals of the tilted cylinders corresponds to 180° minus the X-angle observed in the SAXS experiments (Figure 9).

SAXS on this irradiated and fixed sample helps to connect the real space TEM projection with the dynamic SAXS patterns. Figure 6 (top row) compares the optical transform (OT) (b) and the SAXS pattern (c) corresponding to the image in part a. The slightly larger X-angle of the OT pattern (58°) as compared to the SAXS pattern (54°) indicates that the particular region in a has a somewhat larger than average chevron angle. The X-angle in the SAXS pattern c corresponds to a deformation of approximately 100% in the unloading curve in Figure 14a of ref 1, which agrees fairly well with the macroscopically measured 120% deformation. As the final fixed deformation is always less than the holding deformation after irradiation, the unloading curve of Figure 14a in ref 1 is the more appropriate relationship between the macroscopic deformation and the X-angle. TEM images and OTs support the notion that there is a finite distribution of chevron angles in the irradiated sample.

5.2. 180% Strain—Perpendicular View. TEM at normal incidence in Figure 6d shows that the higher deformation results in a smaller chevron angle (compare 6d to 6a). This particular sample was stretched slightly asymmetrically, i.e., the applied force direction was not

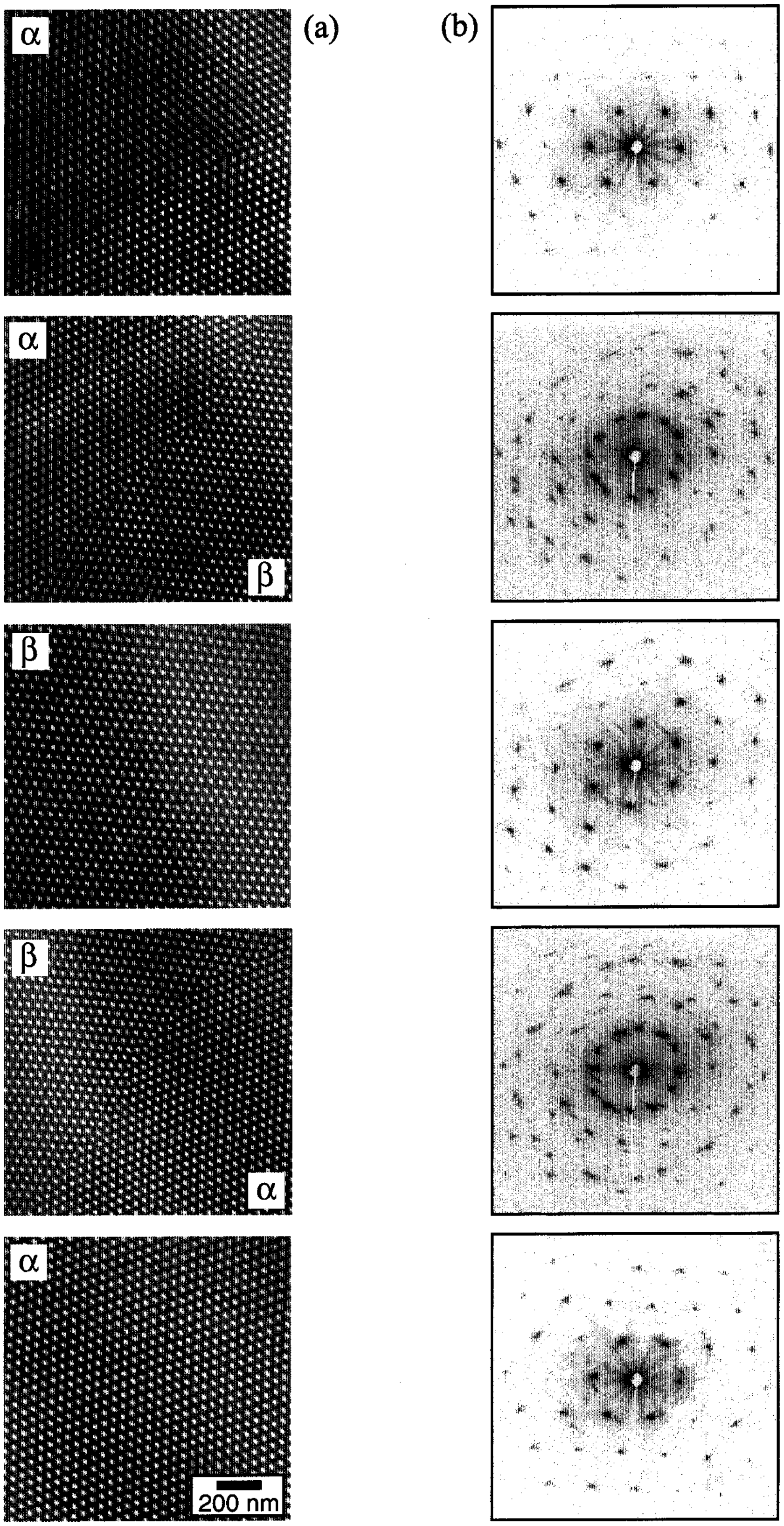

Figure 4. TEM micrographs at parallel incidence (a) and their corresponding OTs (b). The images are from a contiguous region in which the grains (α, and *β*) are directly adjacent to one another. The OTs of the interfaces (α/*β* and *β*/α) indicate how rotational misorientation contributes to the SAXS pattern in Figure 10a of ref 1. The angle of misorientation between grain α and grains *β* is approximately 25°.

exactly normal to the cylinder axis. Figure 6e and 6f show the corresponding SAXS pattern and OT of the same TEM area. Comparison of 6e with the OT in Figure 6b indicates that the X-angle is larger in the HVL sample than in the Raychem sample. Additionally, the X-angle measured via SAXS (86°) corresponds to a permanent deformation of approximately 170% using the unloading curve in Figure 14a of ref 1, which again agrees well with the macroscopically measured permanent deformation.

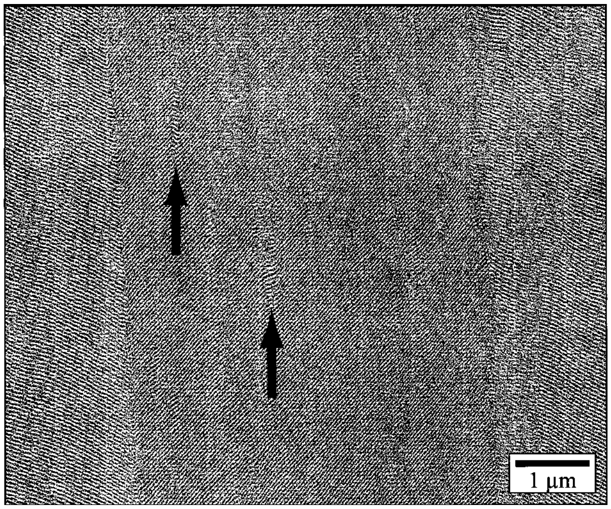

Figure 5. Low magnification image showing a kink band from a sample permanently deformed to 120% strain (Figure 6a). The two kink boundaries are sharp and oriented along the stretching direction. The small vertically oriented subgrains within the central kink band (arrowed regions) are asymmetric kink bands.

There are a number of similarities between the SAXS pattern and OT of the irradiated sample and with the X-patterns observed during the dynamic in-situ SAXS-deformation experiments. In all the types of patterns, the strongest peak in each arm of the pattern is the second one, which in the dynamic experiments is known to correspond to the $(\bar{1}2\bar{1}0)$ $(\sqrt{3})$ peak.[1] Also the first peak is weak in the SAXS pattern of Figure 6c and also very faint in the OT (part b). A second similarity is the observation that the peaks making up the two parallel arms of the X are not collinear across the origin. Because of the mutual location of the Bragg peaks and the Ewald sphere for the incident beam along the y direction, deformation causes the $(10\bar{1}0)$ peak to move away from the Ewald sphere. However, the intensity of this peak is not completely lost because the deformation induces thin, elongated faults that cause streaking of the $(10\bar{1}0)$ peak in a direction parallel to the y axis (see next section, Figure 7, parts d, c, and f, and Figure 9). The elongated $(10\bar{1}0)$ peak still intersects the Ewald sphere (xz plane), leading to a weaker reflection which is noncollinear with the origin and the $(\bar{1}2\bar{1}0)$ peak (which remains on the $x-z$ plane before and after X pattern formation—Figures 9 and 10). Establishing the similarity between the X pattern in the SAXS of the irradiated sample and those observed in the dynamic experiments enables a self-consistent model of the deformed structure to be built on the basis of the TEM projections (see discussion).

5.3. 120% Strain—Parallel View. Though the images at 120% and 180% deformation in the perpendicular view are similar (Figure 6), this is not the case for the parallel view. Figure 7a shows the distorted hexagonal lattice resulting from a deformation history in which the sample was initially stretched to 620%, irradiated, and subsequently unloaded to a final (and

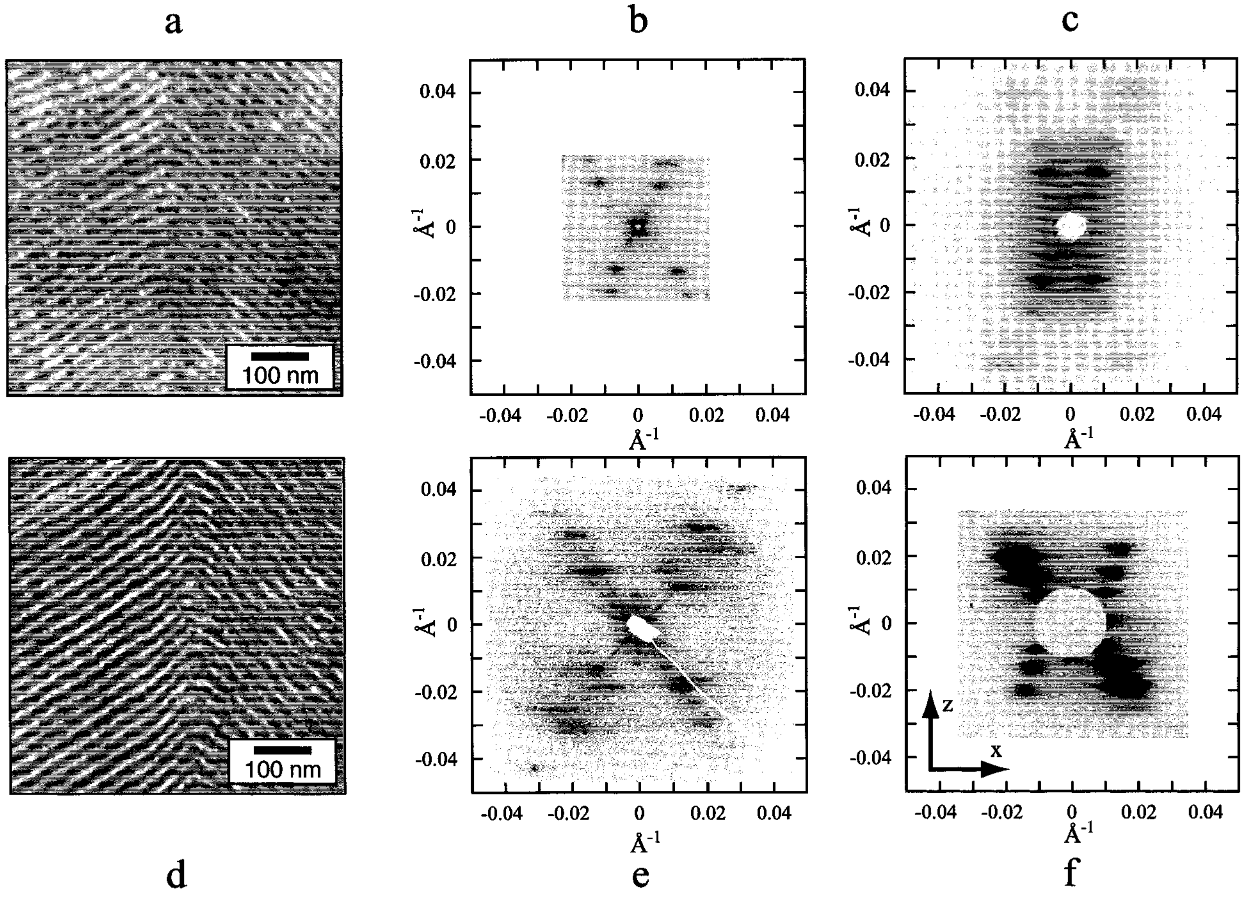

Figure 6. TEM image (a, d), OT (b, e), and SAXS (c, f) of samples stretched to 120% (top) and 180% (bottom) viewed at perpendicular incidence, respectively. The initially straight PS cylinders have bent into a chevronlike texture by the deformation. With increasing deformation the chevron angle becomes more acute; at 120% strain the X-angle is approximately 68° (a) while at 180% strain it is 85° (d). The X-angle increases with increasing deformation as can be seen by comparing the corresponding OTs (b and e) and SAXS patterns (c and f).

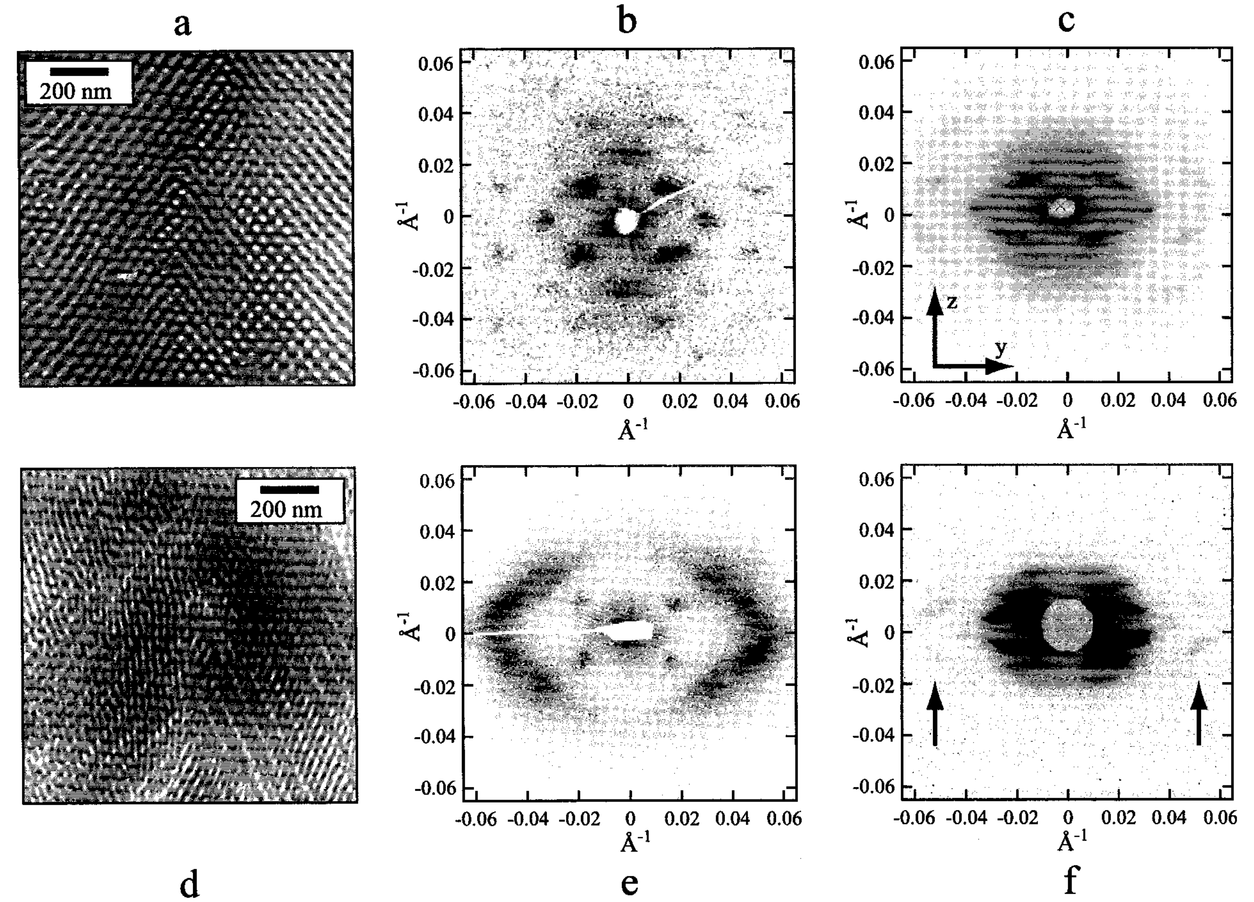

Figure 7. TEM image (a, d), OT (b, e), and SAXS (c, f) of samples with deformations of 120% (top) and 180% (bottom) viewed at parallel incidence, respectively. At 120% the cylinders align in layers with two dominant orientations with respect to the stretching direction (SD) separated by a fault boundary (a). The OT (b) shows well-separated peaks indicative of the underlying distorted hexagonal lattice of the TEM image. At 180% strain, layers with internal contrast modulations are clearly oriented at well-defined angles with respect to the SD (d). The two orientations are separated by a fault boundary aligned in the SD. The OT (e) contains information at two length scales, the spacing and orientation of the layers in the low *q* peaks, and the correlation between contrast modulations within each layer in the high *q* diffuse scatter. The SAXS patterns (c and f) of the deformed samples allow the connection to the dynamic deformation experiments of ref 1. Note the general correspondence of the features in the OT and SAXS patterns.

permanent) deformation of 120%. The SAXS pattern and the OT of the TEM image corresponding to the irradiated sample are shown in Figure 7, parts b and c. These patterns indicate that the extent of deformation corresponds to that between that at 60% and 140% in Figure 8 of ref 1, consistent with the macroscopically measured 120% strain. The original hexagonal lattice has been distorted, but the lateral contraction along the horizontal direction is not uniform. Parts of the image show white dots indicative of projections down the cylinder axis. Other parts of the TEM image show modulated white layer lines. These layers have two dominant orientations with respect to the SD. They impinge to form planar boundaries parallel to the applied force that are reminiscent of twin boundaries (see Figure 7a, center). But since a twin boundary is characterized by a twinning plane and a twin axis,[26] the grain boundaries viewed at parallel incidence cannot be called twin boundaries in the strict sense as the lattice is not clear enough at the boundary to discern both a twinning plane and a twinning axis. We therefore denote them as fault boundaries to indicate the relative translation across the boundary.

The OT of Figure 7b reflects the lattice order which is retained in the deformed morphology depicted in Figure 7a. A distorted hexagonal diffraction pattern can be recognized. The SAXS pattern of the irradiated sample in Figure 7c, though showing less distinct lattice order, can be related to the OT of Figure 7b. The strongest four arced reflections nearest the origin in c correspond to the four strong inner peaks in b and the pair of peaks on the equator in 7c match those of 7b.

5.4. 180% Strain—Parallel View. Examination at parallel incidence of the sample with 180% permanent deformation also shows more faulting than for the sample with 120% permanent deformation (i.e., compare Figure 7d to Figure 7a). Figure 7d shows a parallel incidence micrograph clearly showing an “up” fault boundary at a fairly acute fault angle of 78°. The distorted hexagonal lattice seen in Figure 7a is no longer distinguishable. The similarity of the 2-D SAXS pattern of the irradiated sample in Figure 7f is consistent with 2-D SAXS patterns from the dynamic stretching experiment.[1] The OT in Figure 7e shows information at two length scales. At low values of *q*, the four sharp spots correspond to the spacing between the layers. These spots are equivalent to the four strong peaks in the SAXS pattern of Figure 7f. At high values of *q*, the four inclined streaks above and below the equator arise from the modulations within the layers. The streaking is due to the weak correlation of the modulations within the layers.

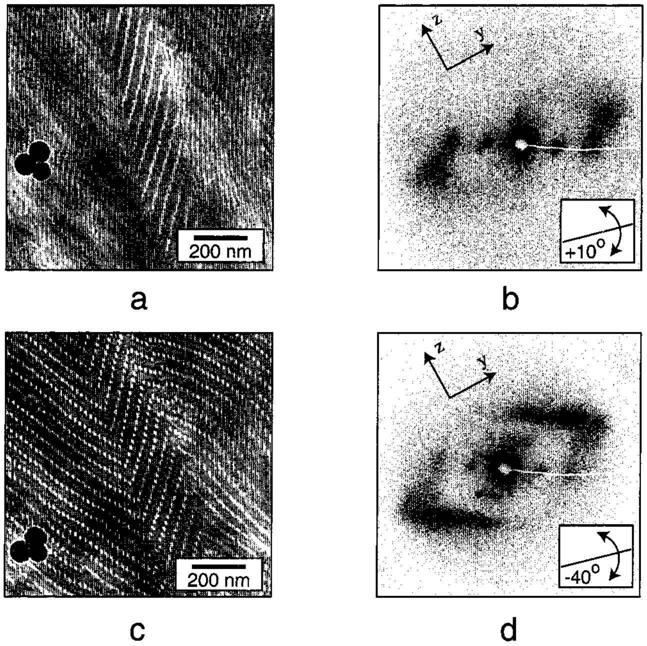

Figure 8. Tilt pair of a sample with 180% deformation viewed at parallel incidence (0° tilt). At +10° tilt, a complex pattern of dark layers with both large and fine spacings are observed in the TEM image (a). The corresponding OT (b) demonstrates the presence of only one set of large well-ordered spacings in a pair of low *q* peaks and a multitude of less well-correlated finely spaced layers in diffuse scatter at high *q*. Tilting about the indicated tilt axis results in the observation of white dots aligned in two sets of layers oriented at a particular angle with respect to the SD (c). The boundary planes (fault boundaries) between the layers are aligned in the SD (*z* axis). The OT (d) is essentially identical to that of Figure 7e enabling a clearer interpretation of the TEM image in Figure 7d (see text).

In both pairs of figures (Figure 7, parts b and c, and (Figure 7, parts e and f), the difference between the SAXS pattern and the OT is due primarily to a difference in sampling volume. The difference in sampling volume between TEM and SAXS is enormous. A typical micrograph contains approximately 10 μm^2 of sample area, which, at a section thickness of 0.1 μm, represents a volume of approximately 1 μm^3. In contrast, a typical SAXS experiment probes a volume of 1 mm^3, an approximately 10^9 times larger volume of material. Despite this difference in sampling volume, however, the essential elements of the lattice distortion at parallel incidence are common to both sets of reciprocal space data. In Figures 7b and 7c, the peaks making up the $\{10\bar{1}0\}$ peak family are present in both SAXS pattern and OT, though in the former case there is much more streaking of the four nonequatorial peaks in the *y* direction. In Figures 7e and 7f, the four strong inner peaks in the OT correspond to the four most intense (and broadened) $(10\bar{1}0)$ peaks in the SAXS pattern. The diffuse scatter at high *q* observed clearly in the OT in Figure 7e corresponds to the four faint peaks at the edges of the SAXS pattern in Figure 7f (arrowed). The $(10\bar{1}0)$ peaks along the equator are almost entirely suppressed by the zero of the form factor in the SAXS pattern and are altogether missing in the OT.

5.5. Tilt Series at 180% Strain—Parallel View. The full X-ray pattern is a 3-D Fourier transform of electron density variations of the bulk sample. The 2-D SAXS pattern is a central section of this 3-D scattered intensity distribution. On the other hand, the TEM image results from a projection through the thickness of the 3-D osmium tetroxide selectively enhanced density distribution of the thin sample. Thus, except for the global vs local difference in the volume sampled (a factor of 10^9), the optical transform of the TEM image corresponds to the SAXS pattern when the incident X-ray beam in the SAXS experiment is along the same direction as the electron beam in the TEM experiment.

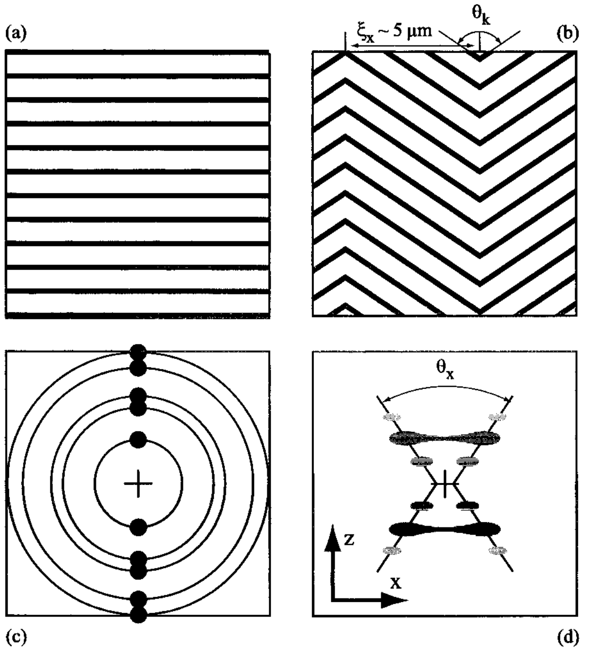

Figure 9. 2-D schematics of the cylinder morphology viewed normal to the cylinder axis before (a and c) and after (b and d) the kinking transition in real (a and b) and reciprocal (c and d) space. Though the tilt boundaries are spaced aperiodically, a correlation width (ξ_x) is estimated at approximately 5 μm (b). The kink angle (θ_k) is related to the X-angle (θ_x) by $\theta_k = 180 - \theta_x$. The initial SAXS pattern contains every allowed reflection for the hexagonal symmetry associated with the cylinder morphology indicative of some axial misorientation (c).[1] The fully developed X-pattern (d) is made up of two pairs of noncollinear arms. Each reflection becomes streaked in the *x* direction due to either the finite width of the kink bands or slight variations in kink angle. The second ($\sqrt{3}$) peak in each arm becomes the strongest reflection with deformation as it remains in the $x-z$ plane (see Figure 10f).

Tilting the TEM section clarifies the origin of the contrast modulations within the layers. Figure 8 shows a tilt pair of micrographs and their corresponding OTs. The layered structure with contrast modulations is observed at a tilt of +10°. The OTs are, however, asymmetric as one set of layer lines are obscured by overlapping cylinders. At a tilt angle of −40° the modulations have resolved themselves into circular white dots indicative of a projection down the cylinder axis (Figure 8c). The OT has gained the other pair of the four inner spots as well as the outer streaks and become symmetric. It is clear from the tilt series that the cylinders are no longer oriented with their axes along the TEM section thickness direction, but have all been tilted by the deformation. The amount of tilt relative to the thickness of the section is such that a normal incidence TEM projection will result in an image made up of overlapping white (PS) and dark (stained rubber) regions. It is only because the spacing between cylinders in the stretching direction is so much larger than any other spacing that a layered structure is observed. The cylinders within the layer are spaced too

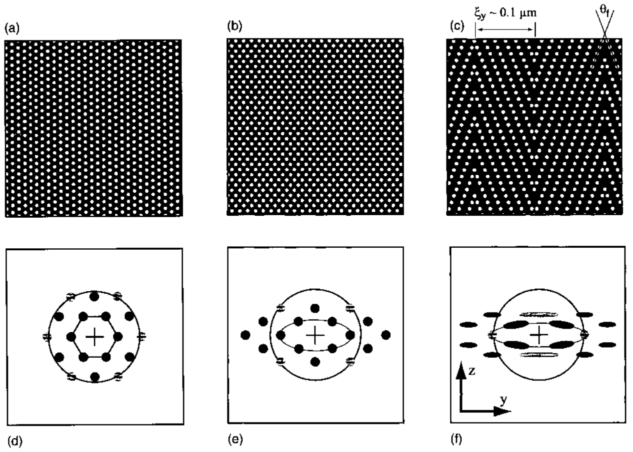

Figure 10. 2-D schematics of the cylinder morphology viewed parallel to the cylinder axis before (a and d) and after deformation (b, c, e, f) in real (top) and the corresponding reciprocal space (bottom). The undeformed real and reciprocal space pair (a and d) are deformed homogeneously to yield the pair b/e. The faulting of the distorted hexagonal lattice in c is supported by the data of Figure 8c. The effect of the faulted texture shown in c on the reciprocal space pattern in part f is indicated by peak streaking. A homogeneous deformation as in b/e would not induce such peak broadening. As the SAXS data in ref 1 shows a continuous $(\bar{1}2\bar{1}0)/(1\bar{2}10)$ peak broadening with increasing deformation, faulting is thought to ocurr in a continuous fashion. The fault boundaries are aperiodically spaced, a correlation width (ξ_y) is estimated at approximately 0.1 μm. The effect of the zero of the form factor (denoted by the constant-diameter circle) on peak intensity is indicated by gray-shading of peaks. The inner hexagon in d distorts into an ellipse in e and f. The $(\bar{1}2\bar{1}0)$ and $(1\bar{2}10)$ peaks move out of the $y-z$ plane (see Figure 9d) giving a lower intensity (gray streaks).

closely to be distinguished at normal incidence and it is only by tilting the section with respect to the incident beam that the overlap is reduced to an extent that the individual cylinders can be resolved. The resolved cylinders appear circular in cross-section, consistent with the invariance of the cylinder form factor zero during stretching.[1] The pattern of cylinders is chevron-like in nature, with cylinder-layers oriented at fixed angles with respect to the SD. The boundaries between the tilted cylinders are well-defined, but since the cylinders themselves do not traverse the fault planes, they are not significantly affected. The spacing between fault boundaries is much smaller and more variable (average value on the order of 0.1 μm) than the chevron boundaries observed in the perpendicular view.

6. Discussion

6.1. Perpendicular View. At lower magnifications in the TEM, it is possible to visualize the larger structure of the chevrons. For both the Raychem and the HVL samples, montages of many closely spaced negatives were constructed yielding a contiguous field of view of approximately 22 × 20 and 29 × 20 μm^2, respectively. From such images, it is evident that the chevron boundaries remain straight and aligned with the stretching direction. The tilted cylinder regions are not uniform but contain small subgrains (arrows in Figure 5) which occasionally interrupt the cylinder trajectory. Figure 9 shows 2-D schematics of the cylinder structure before and after deformation beyond the kinking transition in both real and reciprocal space. The 2-D real space model of the deformed structure (Figure 9b) is consistent with the reciprocal space schematic of the X pattern (Figure 9d). The X-angle (θ_x) equals 180° minus the chevron angle (θ_k). The spacing between tilt walls in the chevron pattern is aperiodic; an average distance (correlation length) is estimated to be approximately 5 μm.

From the TEM images we see that the PS cylinders at the tilt boundary do not fracture. Both the dimensional constraint and the relative low molecular weight of the PS contribute to a weaker resistance to deformation than is typical for bulk PS. The PS acts as a hinge undergoing plastic deformation as the X angle increases. The resistance of the PS to deformation during unloading is less than during loading due to the Baushinger effect of PS, an anisotropy of work-hardening often found in metals where for example, work-hardening efficiency on stress reversal is lower.[27] The Bauschinger effect in PS may help account for the hysteresis in the X-angle curve during unloading (Figure 14a of ref 1). The relatively small amount of deformation at the tip of the bent cylinders might explain the fact that structurally, the sample recovers almost to its initial state (approximately 5% residual deformation; see Figures 5 and 7 of ref 1).

The perpendicular view of the deformed morphology represents the first direct imaging of the chevron texture for cylinders deformed normal to their axes.[4] Previous investigations primarily used SAXS, an indirect technique, to reach the conclusion that the cylinders must kink into a chevron structure. Several investigators have been able to image chevrons in deformed lamellar systems via TEM.[15,18,21] The greater challenge in the cylinder morphology lies in capturing a significant amount of strain. Lamellar systems, with their higher PS content and 2-D constraint, kink at lower strains (~5−10%),[21] show greater hysteresis and less extensibility, which facilitates preserving a permanent deformation during TEM preparation.

As discussed in ref 1, the cylinders kink due to some combination of matrix shear instability and cylinder buckling instability. Regions of misaligned cylinders kink as a result of a resolved shear brought about by the axial compression. Alternatively, aligned cylinders buckle when the buckling stress is exceeded. The nonperiodic kink bands suggest that kinking does not occur uniformly as implied by a buckling mechanism. The kinking stress is thus controlled by the extent of cylinder misalignment, the shear resistance of the matrix as well as the resistance of the PS cylinders to bending.

An analogy to kink band formation in lamellae diblocks undergoing large amplitude oscillatory shear has been drawn to the kinking transition observed here in the cylinder morphology.[28] The mechanism presented to explain kink band formation in lamellar diblocks is one of a preferential slip parallel to the lamellae which causes a region of the lamellae to rotate into the shearing direction when a shear strain exceeds a critical value.[28] The rotated region represents a kink band separated from the unkinked remainder of the sample by sharp boundary walls. The basic mechanism of kink band formation seems to be operative in the kinking transition observed here, namely "layer slip and limb rotation."[28] One main difference is that the cylinders turn toward the SD symmetrically about the tilt boundaries, whereas kink band formation and orientation in sheared lamellar melts depend on the direction and magnitude of the shear.

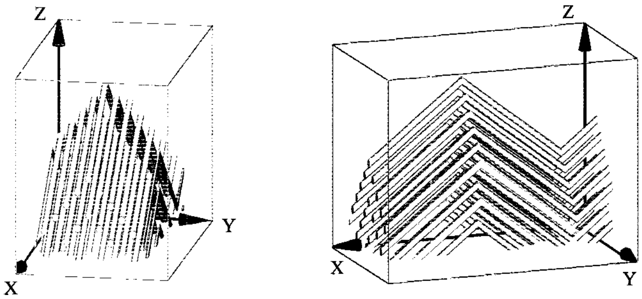

Figure 11. Two perspective views of a 3-D schematic model of the structure deformed to approximately 180%. The cylinders are kinked in the *xz* plane, whereas the cylinders have faulted in the *yz* plane. The cylinders move cooperately to maintain a high degree of order even at the large (>500%) deformations.

A recent investigation[29] has postulated a 2-D model for the kinking transition to proceed via a buckling instability in which the glassy layers form sinusoidal undulations that quickly develop into more sawtoothlike contours. The textures observed in the present TEM micrographs do not show any evidence of a precursor sinusoidal cylinder profile.

6.2. Parallel View. The structure, when examined at parallel incidence (along the *x* direction), is complicated by the discrete nature of the cylinders in the *y*−*z* plane. At large deformations the hexagonal lattice is not only distorted by the deformation but also undergoes a type of faulting in the lateral packing of the cylinders, which gives rise to a second chevronlike texture (see Figure 8c). Figure 10 attempts to clarify this structure. The cylinders have arranged themselves into layers which appear reminiscent of twin boundaries often found in atomic crystals (Figure 10c). A uniform vertical extension and lateral compression do not in themselves give rise to fault boundaries (Figure 10b). It is unclear what causes the strain localization associated with fault boundary formation. Lattice defects such as axial grain boundaries (Figure 3) and axial dislocations (Figure 2) are expected to play a role.

The faulting at parallel incidence is indicated by the gradual development of streaking of the (1$\bar{1}$00), (1$\bar{1}$00), (0$\bar{1}$10), and (01$\bar{1}$0) peaks (see Figures 4 and 8 of ref 1 and Figure 10f). The faulting of the distorted lattice (cylinders undergoing shifting in the SD) to pack into a layered structure (Figure 10c) is expected to be an even more diffuse and continuous process than kinking and to absorb little plastic strain energy. The onset of faulting most likely occurs before the kinking transition as there is no evidence of a second discontinuity (the first being the kinking transition) in the variation of the interplanar spacing observed at parallel incidence in the dynamic SAXS data.[1]

6.3. 3-D Model of the Deformed Morphology. The real and reciprocal space data at large deformations can be assembled into a 3-D model of the deformed structure. Combining the two 2-D models (Figures 9b and 10c) with the fact that the cylinders do not rotate out of the *yz* plane[22] enables a 3-D schematic of the deformed morphology to be drawn (Figure 11). All of the bent cylinders within a band are "in phase" with one another so that the lateral packing (in the *y* direction) is not constrained by the bending. Within a fully kinked region the cylinders turn cooperatively to minimize chain stretching. The PS domains on either side of the tip of the bend are kept in close proximity by the surrounding matrix chains some of which may even span the bend. The intercylinder spacing has increased along *z* and decreased along *y*.

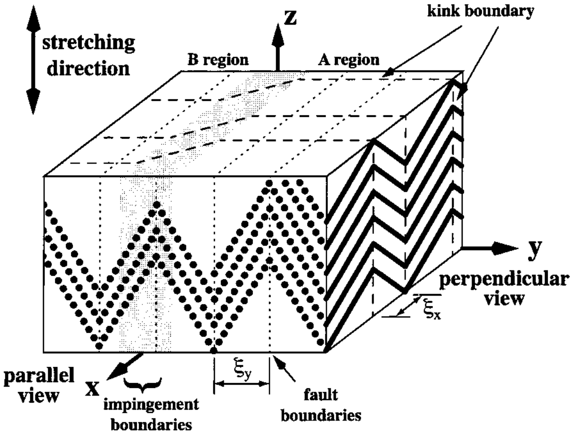

Figure 12. 3-D schematic model showing the perpendicular deformation of the cylinder morphology at high strain. The structure consists of regions of parallel cylinders with kink boundaries and fault boundaries parallel to the stretching direction. Two regions (region A at $y > 0$ and region B at $y < 0$) have kinked independently of one another. The gray area represents the volume over which the tilt boundaries shift in the *x* direction to link-up. The lattice in the *x*−*z* plane readily accommodates these tilt boundary shifts by forming fault boundaries as needed. The scale along the *x* axis has been reduced by approximately 50×.

Figure 12 attempts to place the cooperatively kinked region depicted in Figure 11 within a somewhat larger representative volume element. The kinked PS rods are observed by viewing along y (perpendicular view). The kink boundary is a plane parallel to the *yz* plane (dashed line). The cylinder packing of Figure 10c is repeated in the *yz* plane of Figure 12. The fault boundaries separating layers of cylinders tilted into the stretching direction (*z*) are indicated by dotted lines in the *xz* plane. The ratio of the correlation lengths separating kink and fault boundaries, respectively, is approximately 5 μm/0.1 μm or a factor of 50. Because of the large aspect ratio of the correlation lengths, Figure 12 is not drawn to scale.

Because of various types of misalignment, the kinking is not expected to occur simultaneously and uniformly throughout the volume of the sample. Rather, areas of the greatest cylinder misalignment most likely serve as nucleation sites forming regions of bent cylinders. These regions are uncorrelated. Upon further deformation and transformation of more of the undeformed material into kinked cylinders, kinked regions will begin to impinge. To minimize the elastic strain energy at these impingement "boundaries", the cylinders accommodate the misregistry and form diffuse grain boundaries (gray region in Figure 12).

7. Conclusions

A poly(styrene−isoprene−styrene) triblock copolymer with a cylindrical morphology was oriented via roll-casting. Samples were stretched normal to the cylinder axis and cross-linked by high energy electron irradiation in order to retain the deformed morphology. TEM imaging with the incident beam perpendicular and parallel to the original cylinder axis provide local information on the deformed morphology. The perpendicular view reveals that, at deformations of 120% and 180%, the cylinders are arranged into a chevron pattern consisting of symmetric kink boundaries. Optical transforms (OTs) of the images and SAXS of the irradiated samples provides the basis for an interpretation for the X pattern observed previously via SAXS.[1] Increasing the deformation results in a larger X-angle. The parallel view illustrates how the original hexagonal lattice distorts with increasing deformation. At 120% the lattice within a kink band has an orthorhombic symmetry with evidence of incipient faulting. At 180% the fault boundaries become quite clear, though the 2-D lattice is no longer recognizable in the parallel viewing direction. By performing a tilt series on the 180% sample, the cylinder arrangement becomes clear. The cylinders are lined up into rows which are oriented at a fixed angle with respect to the stretching direction (SD). The boundaries separating rows tilted up from those tilted down are reminiscent of twin boundaries without a clear crystallographic relationship between the two orientations. Thus, they are termed fault boundaries. The deformed cylinders remain circular in cross-section.

The two orthogonal TEM views of the structure are combined into a 3-D model of the deformed morphology, which serves as the basis for the interpretation of the SAXS data reported in the accompanying paper.[1]

Understanding of the deformation process in globally oriented systems is a precondition for a deeper understanding of the deformation of unoriented systems. The response to applied deformation of a polygranular system is a synthesis of the individual responses of each grain together with the boundary conditions imposed by compatibility. The main features of the deformation process of the two principal directions for globally oriented styrene−diene triblock copolymers are now established. Keller and Odell demonstrated how deformation along the cylinder axis leads to breakup and fragmentation of the cylinders.[17] We have seen how deformation perpendicular to the cylinder axis leads to kinking and faulting. Deformation applied at other angles will lead to a response combining elements of both processes. At small angles from the cylinder axis, fragmentation is expected to dominate. At angles near 90°, kinking is expected to dominate. The response at intermediate angles is expected to involve asymmetric kinking and/or fragmentation depending critically on the angle of the applied deformation. It remains for us to investigate the impact of grain boundaries and grain size on the morphological response and thus the mechanical properties.

Acknowledgment. This work was supported by grants from NSF: DMR 98-01759 and MRSEC MIT facilities. We thank Dr. W Johnson and Mr. M. J. Repogle at Raychem (now Tyco Electronics) for their contributions to the irradiation of the samples. C.C.H. thanks Prof. A. Argon and Prof. D. C. Martin for helpful discussions. Dr. B. Walters of Dexco is acknowledged for providing the material. Prof. S. Gruner, Dr. D. A. Hajduk, and Dr. M. Capel are thanked for their help in obtaining the SAXS patterns in Figures 6 and 7.

References and Notes

(1) Honeker, C. C.; Thomas, E. L.; Albalak, R. J.; Hajduk, D. A.; Gruner, S. M.; Capel, M. C. *Macromolecules* **2000**, *33*, 9395.
(2) Rader, C. P. *Modern Plastics: Encyclopedia 1997*; McGraw-Hill Co.: New York, 1996; Vol. 73; p B51.
(3) Holden, G.; Bishop, E. T.; Legge, N. R. *J. Polym. Sci. C* **1969**, *26*, 37.
(4) Honeker, C. C.; Thomas, E. L. *Chem. Mater.* **1996**, *8*, 1702.
(5) Fetters, L. J.; Thomas, E. L. *Materials Science and Technology: A Comprehensive Treatment Vol. 12: Structure and Properties of Polymers*; VCH: Weinheim, 1993; Chapter 1: Model polymers for materials science.
(6) Arridge, R. G. C.; Folkes, M. J. *J. Phys. D: Appl. Phys.* **1972**, *5*, 344.
(7) Albalak, R. J.; Thomas, E. L. *J. Polym. Sci., B: Polym. Phys.* **1993**, *31*, 37.
(8) Albalak, R. J.; Thomas, E. L. *J. Polym. Sci., B: Polym. Phys.* **1994**, *32*, 341.
(9) Tarasov, S. G.; Tsvankin, D. Y.; Godovsky, Y. K. *Polym. Sci. USSR* **1978**, *20*, 1728.
(10) Pakula, T.; Saijo, K.; Kawai, H.; Hashimoto, T. *Macromolecules* **1985**, *18*, 1294.
(11) Hendus, H.; Illers, K.-H.; Ropte, E. *Colloid Polym. Sci.* **1967**, *216*, 6−217, 110.
(12) Beecher, J. F.; Marker, L.; Bradford, R. D.; Aggarwal, S. L. *J. Polym. Sci. C* **1969**, *26*, 117.
(13) Pedemonte, E.; Dondero, G.; Alfonso, G.; de Candia, F. *Polymer* **1975**, *16*, 531.
(14) Pedemonte, E.; Dondero, G.; de Candia, F.; Romano, G. *Polymer* **1976**, *17*, 72.
(15) Fujimura, M.; Hashimoto, T.; Kawai, H. *Rubber Chem. Technol.* **1978**, *51*, 215.
(16) Hashimoto, T.; Fujimura, M.; Saijo, K.; Kawai, H.; Diamant, J.; Shen, M. In *Multiphase Polymers*; Cooper, S. L., Estes, G. M., Eds.; ACS Advances in Chemistry Series; American Chemical Society: Washington, DC, 1979; p 257.
(17) Odell, J. A.; Keller, A. *Polym. Eng. Sci.* **1977**, *17*, 544.
(18) Yamaoka, I.; Kimura, M. *Polymer* **1993**, *34*, 4399.
(19) Yamaoka, I. *Polymer* **1996**, *37*, 5343.
(20) Yamaoka, I. *Polymer* **1998**, *39*, 1081.
(21) Cohen, Y.; Albalak, R. J.; Dair, B. J.; Thomas, E. L. *Macromolecules* **2000**, *33*, 6502.
(22) Honeker, C. Ph.D. Thesis, Massachusetts Institute of Technology, 1997.
(23) Klier, I. *J. Polym. Eng.* **1997**, *16*, 311.
(24) Lyons, B. J.; Johnson, W. C. In *Irradiation of Polymeric Materials*; Reichmanis, E., Ed.; Advances in Chemistry Series 527; American Chemical Society: Washington, DC, 1993; p 62.
(25) Johnson, W. C.; Lyons, B. J. *Radiat. Phys. Chem.* **1995**, *46*, 829.
(26) Cullity, B. D. *Elements of X-ray Diffraction*; Addison-Wesley: Reading, MA, 1978; p 555.
(27) Argon, A. S.; Backer, S.; McClintock, F. A.; Reichenbach, G. S.; Orowan, E.; Shaw, M. C.; Rabinowicz, E. *Mechanical Behavior of Materials*; Addison-Wesley: Reading, MA, 1966.
(28) Polis, D. L.; Winey, K. I. *Macromolecules* **1998**, *31*, 3617.
(29) Read, D. J.; Duckett, R. A.; Sweeney, J.; McLeish, T. C. B. *J. Phys. D: Appl. Phys.* **1999**, *32*, 2087.
(30) McGinniss, V. D. *Encyclopedia of Polymer Science: Crosslinking with radiation*; John Wiley & Sons: New York, 1986; Vol. 4, p 418.

MA000594Q